Exploiting cryo-EM structures of actomyosin-5a to reveal the physical properties of its lever

Authors: Molly S.C. Gravett [1], David P. Klebl [1], Oliver G. Harlen [2], Daniel J. Read [2], Sarah A. Harris [1], Stephen P. Muench [1], Michelle Peckham [1]

[1] Astbury Centre for Structural Molecular Biology, University of Leeds, Leeds, UK

[2] School of Mathematics, University of Leeds, Leeds, UK

Abstract

Myosin 5a transports cellular cargos along actin filaments towards the cell periphery. Its long lever plays a key role in determining the large size of its powerstoke, stepping distance along F-actin, ability to bear load and its regulation by Ca^{2+}. Despite this, little is known about the physical properties of the lever and how they contribute to the mechanics of walking. Using a combination of cryo-electron microscopy and molecular dynamics simulations, we resolved the first structure of myosin 5a comprising the motor domain and full-length lever (subfragment-1) bound to actin. From the flexibility captured in the cryo-electron microscopy data, we were able to characterise the stiffness of the lever. Here, we demonstrate how the structure and flexibility of the lever contribute to the regulation and walking behaviour of myosin 5a.

Introduction

Myosins are a family of motor proteins that use ATP hydrolysis to drive movement along a filamentous actin (F-actin) track. The myosin superfamily is made up of approximately 80 classes with a diverse array of functions, such as vesicle transport, muscle contraction and membrane tethering (Foth et al., 2006; Hartman and Spudich, 2012; Kollmar and Mühlhausen, 2017). Unconventional myosin 5a (Myo5a) is one of three vertebrate myosin 5 isoforms (a, b & c) (Hammer and Sellers, 2012). It is expressed in pigment producing cells, found in the skin, brain, ears, eyes and hair, called melanocytes (Provance and Mercer, 1999), and Purkinje neurons (Wagner et al., 2011). Myo5a is a non-muscle myosin primarily involved in the transport of cellular cargos along cytoskeletal F-actin to the periphery of cells (Hammer and Sellers, 2012). Such cargos include pigment-containing melanosomes, for protection from ultraviolet radiation (Reck-Peterson et al., 2000), and the endoplasmic reticulum in the dendritic spines of Purkinje neurons, important for motor learning (Wagner et al., 2011). Mutations in Myo5a lead to the pigmentation and neuronal defects seen in the rare disease Griscelli Syndrome (Mercer et al., 1991; Pastural et al., 1997; Van Gele et al., 2009). Myo5a has also been implicated in cancer progression (Lan et al., 2010; Alves et al., 2013).

Myosins are multimeric protein complexes consisting of heavy and light chains. The heavy chain of Myo5a is composed of an N-terminal motor domain, followed by a light chain binding domain (LCBD), a coiled-coil forming domain and a cargo-binding domain. The N-terminal motor domain contains both the nucleotide and F-actin

binding sites. Small-scale conformational changes in the motor are amplified to large-scale motions by the lever. The lever is made up of the converter, the LCBD and bound calmodulin (CaM) light chains. The motor and the lever together comprise the myosin head. The head is followed by a coiled-coil forming domain, which dimerises and the C-terminal cargo binding domain recruits Myo5a to its preferred cargo (reviewed in (Titus, 2018)).

The ability of Myo5a to transport cargo depends on its ability to walk processively along F-actin towards the barbed end, taking multiple steps without dissociating. This is facilitated by enzymatic adaptations of the ATPase cycle. In common with other myosins, Myo5a binds to actin with Mg.ADP.P_i in its nucleotide binding site (pre-power stroke state). Next, P_i is released leading to a force-generating movement of the lever (the power stroke), and Myo5a becomes strongly bound to F-actin with only Mg.ADP in the active site (post-power stroke state). Mg^{2+} and ADP are then released from the nucleotide-binding site to form the rigor state (nucleotide free). In Myo5a this is known to result in an additional small change in the lever position (Veigel et al., 2002; Pospich et al., 2021). Mg.ATP then binds to the empty nucleotide binding site in the rigor state, and the motor detaches from F-actin. Importantly, ADP release is the rate limiting step of the ATPase cycle for Myo5a. This means Myo5a spends a large fraction of its ATPase cycle in a state that has a high affinity for F-actin, and this contributes to its high duty ratio (reviewed in (De La Cruz and Ostap, 2004)). In the dimer, when both myosin heads are bound to F-actin, the trail head prevents the lead head from completing its powerstroke following P_i release. This generates strain across the molecule, which reduces ADP dissociation from the lead head by ~250-fold compared to the trail head (a process known as gating (Veigel et al., 2002; Forgacs et al., 2008)). The lead head can therefore only complete its powerstroke when the trail head detaches. This helps to ensure at least one head is bound at any one time, and the preferential release of the rear head helps to bias forward walking.

The long lever of Myo5a is fundamental for its stepping behaviour. It enables Myo5a to walk straight along the longitudinal axis of F-actin, with a step size similar to the helical pseudo-repeat of F-actin (36 nm) (Sakamoto et al., 2003). Moreover, the mechanical properties of the lever must allow transmission of intramolecular strain between the two heads to co-ordinate stepping. The lever of Myo5a is comprised of 6 α-helical IQ (isoleucine-glutamine) motifs, each of which are occupied by CaM. CaMs reinforce the lever domain and are thought to be involved protein-protein interactions and regulation (Heissler and Sellers, 2015). CaM consists of 2 globular regions, the N-lobe (N-terminal) and C-lobe (C-terminal), joined by a flexible linker. The C-lobe forms contacts with the N-terminal region of the IQ motif, and the N-lobe forms contacts with the C-terminal region of the IQ motif (Terrak et al., 2003; Houdusse et al., 2006). The six IQ motifs alternate between 23 and 25 residue spacing. Points of flexion along the lever have been suggested between CaMs bound to 25 residue IQ motifs and the CaMs bound to their C-terminal neighbouring IQ motifs, e.g. CaM-IQ2 (25 residues) and CaM-IQ3 (23 residues). This is thought to be because of increased spacing and reduced CaM-CaM interactions (Terrak et al., 2005). A region of pliancy has also been suggested between the converter and the CaM bound to IQ1 (CaM1) (Houdusse et al., 2000; Burgess et al., 2002).

Despite the important role of the lever in walking mechanics, we currently lack a high-resolution structure of Myo5a with a full-length lever bound to F-actin. High

resolution crystal structures (~2 Å) of short segments of the lever include IQ1-2 (23 and 25 residues) of murine Myo5a bound to CaM (Houdusse et al., 2006) and IQ2-3 (25 and 23 residues) of yeast myosin 5 (Myo2p) bound to myosin light chain 1 (Mlc1p) (Terrak et al., 2005) (PDB: 2IX7 and 1N2D, respectively). A cryo-EM structure of the shutdown state containing the full-length lever was also recently published (approx. 5 Å) (Niu et al., 2022). However, only low-resolution structures of the full-length Myo5a lever in the actin bound active state are available (Walker et al., 2000; Oke et al., 2010). In contrast, the structure of the Myo5a motor domain bound to actin was recently solved to high resolution (approx. 3 Å) for constructs containing the motor domain and the first IQ bound to ELC in both rigor (nucleotide free) and ADP states (Pospich et al., 2021). Therefore, further characterisation of the structural and physical properties of the full-length lever of active Myo5a are required.

Here, we obtained a high-resolution cryo-EM structure (7.5 Å global resolution) of a murine Myo5a construct, comprising the motor domain and a 6IQ lever (Myo5a-S1), to further characterise how the lever of Myo5a contributes to its walking mechanics. In our structure Myo5a-S1 is in the rigor state, bound to F-actin, and each IQ motif in the lever is occupied by a CaM. We generated a pseudoatomic model using all-atom molecular dynamics (MD) simulations in combination with the cryo-EM data to model side-chain conformations. We used the range of conformational heterogeneity in the lever obtained from 9 distinct cryo-EM classes, to determine the overall stiffness of the lever, how the stiffness varies along its length, and to predict the working stroke for Myo5a.

Results and Discussion

Structure of the full-length actomyosin-5a lever by cryo-EM

To determine the properties of the lever in the active state, we have obtained a sub-nanometre cryo-EM structure of Myo5a-S1 bound to F-actin in the rigor state (7.5 Å global resolution) (Figure 1, and Figure 1 Supplement 1A). 3D classification focussing on the lever was used to resolve the whole lever. This was necessary to overcome the high level of particle heterogeneity within the data arising from the intrinsic flexibility of the lever. The focused 3D classification grouped particles based on lever conformation and resulted in 9 distinct classes with density for all 6 CaM-IQs within the lever. The lever conformation varies between the classes, which represent snapshots of continuous motion (see Methods for details). Despite being approximately equally populated, the resolution of each class varied from 7.5 Å-10.7 Å (Figure 1 Supplement 2). Even within the class with the best resolution for the lever, resolution along the lever gradually declined from ~7 to 25 Å, from the converter to IQ6 (Figure 1 Supplement 1B). The reduced resolution towards the end of the lever is likely a result of conformational heterogeneity even within a single class. A pseudoatomic model was generated for this class using all-atom MD simulations (Figure 1B & C, and Figure 1 Supplement 2D), to investigate the arrangement of the bound CaMs and their interactions within the lever.

Focused refinement, where everything outside of 3 F-actin subunits, the motor and the first 2 IQs was excluded, generated a structure that was highly similar to that generated for the motor domain of chicken Myo5a bound to F-actin (Pospich et al.,

2021) and of similar resolution (4.2 Å) (Figure 1 Supplement 3). The conformation of individual subunits (motor and each actin subunit) is the same as that previously reported (Figure 1 Supplement 3A). Differences in the orientation of the motor relative to F-actin (Figure 1 Supplement 3B), may be due to flexibility, species difference, or the use of phalloidin to stabilise F-actin in the earlier report (Pospich et al., 2021).

The N-lobe of CaM6 is dynamic in Myo5a-S1

The cryo-EM density map shows weak density for the N-lobe of CaM6 (Figure 1B & Figure 3). This could be accounted for if the N-lobe of CaM6 is highly mobile, arising from reduced interactions with the IQ domain and the adoption of an extended conformation, as previously predicted (Terrak et al., 2003; Terrak et al., 2005; Black and Persechini, 2010). We therefore used a crystal structure for MLC1P bound to IQ4 of the yeast Myo5 isoform Myo2P, in which the N-lobe of MLC1P does not interact with IQ4 (PDB:1M46, (Terrak et al., 2003)) to build our pseudoatomic model of CaM6. MD simulations demonstrated that N-lobe of CaM6 does have increased mobility in the extended state compared to the compact state seen in CaMs 1-5 (Figure 2). It is therefore plausible that reduced interactions between the N-lobe of CaM6 and IQ6, and the increased flexibility of CaM6 in an extended state, are responsible for the weak of density in the cryo-EM map for the N-lobe of CaM6.

Amino acid substitutions in IQ6 may help to account for the weaker interactions between IQ6 and the N-lobe of CaM (Figure 3). In both Myo5a and Myo2p, the conserved Gly residue at position 7 in IQ6 is replaced by a bulky, charged residue (Arg in Myo5a and Lys in Myo2P). In addition, Arg at position 11 is replaced with Lys (Myo5a) or Gln (Myo2p). It is thought that amino acid substitutions at positions 7 and 11 are responsible for light chains forming an extended state (Terrak et al., 2003). Replacement of Gly7 with Arg in a reference IQ motif weakens its interaction with Ca^{2+} free CaM (apo-CaM) by ~2-fold and is expected to promote the extended state of the N-lobe of CaM, although compensatory electrostatic interactions between Arg and the IQ may occur (Black and Persechini, 2010). In support of this, our pseudoatomic model, and unrestrained MD simulations, show electrostatic contacts do form between Arg7 and Lys11 with the charged N-terminal residues (Glu7 and Asp2, respectively) (Supplementary Table 1, 2 & 3).

In IQ3 of Myo5a, Gly7 is replaced by Met, a bulky and hydrophobic residue. Replacement of Gly7 with Met in a single reference IQ motif weakens its interaction with apo-CaM ~10-fold (Black and Persechini, 2010). Based on this, the N-lobe would be expected to adopt an extended conformation. However, CaM3 adopts a compact conformation in our cryo-EM map (Figure 3C and Figure 1). The presence of neighbouring CaMs may reduce the flexibility of the N-lobe and stabilise interactions between the N-lobe and the IQ motif, suggesting CaMs bind the heavy chain cooperatively. It is possible that under some conditions this lobe could become extended, as a potential strategy for regulating myosin activity, by weakening the lever.

The flexibility seen in CaM6, and its reduced interactions with IQ6, could be important for motor mechanics as plasticity in this region is likely to be necessary for switching between the active and shutdown state. A recent cryo-EM structure of the shutdown inhibited state of Myo5a showed the N-lobes of each CaM6 interact with the coiled-coil to stabilise the sharp bend at the head-tail junction (Niu et al., 2022). Therefore weakened interactions between the N-lobe and IQ6 are likely to be necessary for Myo5a to readily move from the active to the shutdown state. Flexibility at CaM6 may also prevent steric clashes between the two levers at the head-tail junction of dimeric Myo5a. Based on the different behaviour Met substitution has on the CaM bound to a single IQ compared to CaM3 in our lever, the behaviour of CaM6 might be quite different in the dimeric molecule compared to S1 where there is no downstream sequence. High-resolution structures are needed of the head-tail junction in the active dimeric state in order to truly understand the role CaM6 plays.

Flexibility of the lever

Using the ensemble of lever conformations in the cryo-EM 3D classes, we found that the lever of Myo5a has variable stiffness at points along its length. Spring constants for bend and twist at regions between the motor and converter and all 6 CaMs were determined (Table 1 and Figure 4) assuming bend and twist are focused at single hinge points between lever subdomains (Figure 4 Supplement 1). The stiffest connections are between CaM1-2 and CaM2-3. The latter is somewhat surprising as there are limited contacts between CaM2-3 (Supplementary Table 3), and it was previously thought this would be a region of increased flexibility (Terrak et al., 2005). This suggests that the distance between CaM pairs (Figure 4 Supplement 2) and CaM-CaM interactions do not dictate the stiffness at this region. The connections between the converter and CaM1, and CaM3-4 are about half as stiff as CaM1-2 and CaM2-3, while CaM4-5 and CaM5-6 are the most flexible connections. This demonstrates regions of pliancy are distributed along the whole length of the lever rather than being localised at a single ‘pliant point’ between the converter and CaM1 as previously thought (Houdusse et al., 2000; Burgess et al., 2002), although this region is more pliant than its neighbouring connections. No correlation could be found between bending stiffness and subdomain pair conformation, distance or interdomain interactions (Figure 4 Supplement 1, Supplementary Table 1-3). Interestingly, in performing the same analysis of subdomain conformations for previous published structures, we found previous structures fall within the range of subdomain conformations seen within the 3D classes (Figure 4 Supplement 1).

Variable stiffness along the length of the lever is likely to be important for Myo5a mechanics. The lever must be sufficiently stiff to generate intramolecular strain, and to withstand load from cargos without collapsing. The lever must also be sufficiently flexible to accommodate changes in step size, stereospecific binding to actin, and swapping filament track in a F-actin network (Oke et al., 2010; Lombardo et al., 2019). Constructs that have 2 IQ domains but the rest of the lever replaced with a single alpha helix (SAH) can still walk processively, but do not produce intramolecular strain (Baboolal et al., 2009). The stiffness of a SAH is ~50 pN nm, which is ~1/3 the stiffness at hinges between CaM4-6. Taken together this could mean that: some rigidity at the start of the lever is required for translating the powerstroke, some rigidity (at least 3 x SAH stiffness) is required to communicate

intramolecular strain between heads, and that some flexibility exists towards the end of the lever to accommodate for stepping errors.

Using the variance in lever position within the cryo-EM 3D classes and treating the lever as a cantilever, the overall stiffness of the lever was estimated as 0.78 pN/nm for slew motions (across F-actin short axis) and 0.74 pN/nm for tilt motions (bending towards and away from F-actin) (Figure 5). Since the difference is small compared to confidence intervals of these measurements (± 0.3 pN/nm) this suggests that flexibility is directionally isotropic. Additionally, the changes in tilt and slew are uncorrelated, as the correlation coefficient is 0.004, which implies the motion of the lever in these directions is not coordinated. Both of these attributes may be important for strain generation in multiple directions. Equal rigidity in all directions would allow intramolecular strain to be generated between Myo5a heads regardless of their orientation. This may be required in order for Myo5a to walk in either a left- or right-handed manner as seen in interferometric scattering microscopy (iSCAT) and across filaments in an F-actin network as seen in super-resolution stochastic optical reconstruction microscopy (STORM) (Andrecka et al., 2015; Lombardo et al., 2019).

The overall cantilever bending stiffness (0.76 ± 0.07 pN/nm) is similar, but somewhat higher than the stiffness of Myo5a-S1 determined by optical trap measurements (0.2 pN/nm, (Veigel et al., 2002)), dimeric actomyosin-5a by negative stain EM (0.26 pN/nm, (Oke et al., 2010)), the unbound 2IQ Myo2 lever (0.37 pN/nm, (Billington et al., 2014)), and an SAH (0.46 pN/nm, (Sivaramakrishnan et al., 2008)). Our approach is the first direct analysis of Myo5a lever stiffness in 3D, which could account for some of the differences in values between our measurements and other Myo5a-S1 data. It should also be taken into consideration that grouping the cryo-EM data into conformational classes during 3D classification will give rise to a reduced variance compared to looking at individual particles, which results in an increased estimation of stiffness.

Furthermore, the conformations of the lever in the cryo-EM micrographs could be somewhat constrained by the packing of Myo5a-S1 on F-actin. In most of the cryo-EM 3D classes there was additional density corresponding to neighbouring motors (Figure 1 Supplement 2A-F, and H). This could also be a barrier to capturing the full motion of the lever as adjacent levers may interact or clash. However, not all filaments in the micrographs were fully decorated. Future work would involve classifying motors with and without neighbours, to determine the true influence of packing on F-actin on the emergent bending stiffness.

Despite 3D classification and reconstruction reducing the conformational variance that can be observed (relative to the variance obtained if one were able to resolve individual molecules), it is only through this approach that sufficient resolution can be acquired to resolve differences in subdomain conformations and have information in 3D. Therefore, in performing bending stiffness calculations, there is a compromise between the requirement to average particles to allow 3D reconstruction, and the reduction in the conformational variance that comes with it. As the molecule is so flexible, more data is required in order to generate more classes. If, for example, 1000 classes are necessary to perform proper statistical analysis, and ~20000 particles are required for a reconstruction with sufficient resolution to resolve CaMs, 20 million particles would be required to gain the data necessary. This is ~60 times more particles than we acquired, which would mean 60 times more micrographs

(~300,000). Collecting this number of micrographs is starting to become achievable on reasonable timescales with the new fast detectors and automation software, but, together with the large amount of processing required, may be a significant investment that is likely to only modestly improve our estimates.

Lever flexibility accommodates a 35 nm working stroke

Estimations of the Myo5a-S1 working stroke using our cryo-EM 3D classes revealed a 35 ± 6 nm (mean ± SD) working stroke (Figure 6). To model lever conformations in the ADP-P_i and ADP state, the modelled lever domains of each 3D class were superimposed onto the converter domains of a known ADP-P_i and a known ADP structure. The lever end points (residue 914) translate 32 ± 5 nm (mean ± SD) along the F-actin longitudinal axis on average from the ADP-P_i (PDB:4ZG4, (Wulf et al., 2016)) to the ADP (PDB: 7PM5, (Pospich et al., 2021)) state. There was an additional translation of 3 nm along the F-actin longitudinal axis, on average, between the ADP and the rigor state. The total translation of 35 nm along the actin filament is larger than an earlier estimate of the working stroke (28.5 nm), which used a similar approach but looked at lever end-point distances between the states rather than change along F-actin, and was limited to a single lever conformation from the shutdown state (Wulf et al., 2016). Our estimate is also larger than the experimentally measured working stroke for Myo5a-S1 (21 nm) using an optical trap. In the optical trap data the working stroke was comprised of a 16 nm step as Myo5a transitioned from ADP-P_i to ADP, and a further 5 nm step as Myo5a transitioned from ADP to rigor, although the working stroke measured for dimeric Myo5a was longer (25 nm) (Veigel et al., 2002). Previously the differences seen between S1 and the dimer were suggested to be due to differences in how the molecules attach to the nitrocellulose bead in the optical trap assay. However, the difference between S1 and the dimer could be attributed to the leading head in the dimer starting its working stroke from a strained ADP conformation, and not the ADP-P_i state, which we also need to consider in our calculations.

In the 3-bead optical trap, restrictions to the movement of the end of the S1 lever through its attachment to a nitrocellulose bead, together with some uncertainty as to how the lever is attached to the bead, may contribute to an underestimate of the working stroke. Importantly, the previous estimates of the working stroke are much shorter than the step size of 36 nm. This has led to the idea that when the rear head of Myo5a detaches, it has to perform a ~10 nm diffusive search to rebind to the actin filament at the next binding site (Veigel et al., 2002). However, our estimate of the working stroke suggests that this diffusive search would only be a nm, if any (as 1 nm would be within the error). This suggests strain across the molecule is not generated during binding of the new lead head, but only after P_i release, as the lead lever is prevented from entering the post-powerstroke conformation as it is restrained by the trail head.

Conclusion

Here, for the first time, the structure of rigor Myo5a bound to actin with the full-length lever has been resolved with sufficient resolution to distinguish neighbouring CaMs, and their individual lobes. Absence of the N-lobe of CaM6 in the cryo-EM maps, and increased dynamics in the MD simulations, have provided further evidence that the CaM bound to IQ6 can exist in an extended conformation, and its N-lobe has

reduced interactions with IQ6. This is likely to aid formation of the shutdown state and may also be importation for dimerization. Structural resolution of the head-tail junction in the active state is required to further understand the role of CaM at this location.

3D reconstruction of the full-length Myo5a lever domain in 9 different conformations has revealed properties of the lever that contribute to its mechanics. Analysing lever flexibility in 3D, has demonstrated it is directionally isotropic, which may be important for strain generation in multiple directions. Analysing intra-lever flexibility in 3D, has further supported evidence for a hinge region between the converter and CaM1, and revealed a block of rigidity from CaM1-3, followed by a flexible end. Interestingly, no single characteristic, i.e. the conformation of subdomain pairs along a single axis or the number of interdomain interactions seems to correlate with bending stiffness. This suggests that either combined influence of these features encodes stiffness at subdomain connections, or features as yet unexplored.

Variable flexibility along the length of the lever challenges previous hypotheses that assume the lever is a rigid continuous beam. It is possible that 2D ns-EM images of the dimer with both heads bound to F-actin under strain have led to this, as they show a taut lever as opposed to one that can flex and bend (e.g. a tightrope is made of string), which prevents different properties along the length of the lever from being revealed. Whilst, 2D images of the free molecules make it difficult to determine the viewpoint without F-actin as a reference. Additionally, it is hard to determine whether the particles are distorted by the stain in ns-EM. This highlights why 3D reconstruction, despite its shortcomings, is necessary.

Finally, our estimates of the length of the working stroke, using the ensemble of lever conformations within the cryo-EM 3D classes, show Myo5a-S1 is capable of a longer working stroke (~33 nm) than previously described (28.5 and 21 nm) (Veigel et al., 2002; Wulf et al., 2016). A working stroke closer to the length of the F-actin helical pseudo-repeat suggests stepping is more precise than previously thought, and that strain is generated after the motor has bound to F-actin, and P_i has been released. However, for a true understanding of the full working stroke, structural resolution of the lead head in the strained state is required.

Through this analysis we have revealed properties of the lever of Myo5a, and how they contribute to the function of the whole molecule. Many molecular motors beyond Myo5a use light chain bound lever-like domains (Bähler and Rhoads, 2002; Heissler and Sellers, 2015), so this work not only contributes to our knowledge of the mechanism of Myo5a, but may also shed light on how other motor proteins function that share these domains.

Materials and Methods

Sample preparation

Murine Myo5a-S1-6IQ (1-907) and CaM proteins were purified as described in (Wang et al., 2000; Forgacs et al., 2006), and stored in liquid nitrogen (LN_2). Both were kindly provided by Howard White. After thawing stored Myo5a-S1-6IQ, additional CaM was added in a 2:1 ratio to ensure all IQ motifs were fully occupied. Rabbit skeletal muscle G-actin was purified as described in (Pardee and Spudich, 1982). G-actin was dialysed into 0.2 mM $CaCl_2$, 0.5 mM DTT, 0.2 mM ATP, and 2 mM Tris-HCl, at pH 8.0, and stored in LN_2. After thawing, G-actin was polymerised on ice, by first exchanging Ca^{2+} for Mg^{2+} in exchange buffer (final solution concentrations: 1 mM EGTA, 0.27 mM $MgCl_2$) followed by polymerisation in polymerisation buffer (final solution concentrations: 25 mM KCl, 1 mM $MgCl_2$, 1 mM EGTA, 10 mM MOPS, pH 7.0) overnight on ice.

Grid preparation and cryo-EM data acquisition

Quantifoil R2/2 carbon Cu 300 mesh grids (Agar Scientific, Stansted, UK) were glow discharged in an amylamine vapour at 20 mA for 30 s (GloCube, Quorum Technologies Ltd, Laughton, UK). Directly before application, F-actin was sheared by being repeatedly drawn up and ejected with a gel loading pipette tip to shorten filaments, in order to increase the amount of F-actin observed occupying grid holes. 1 µL of sheared F-actin (0.5 µM) was applied to the grid and incubated for 2 mins. 3 µL of Myo5a-S1-6IQ supplemented with CaM (3 µM + 6 µM, respectively) was added to the grid in the Vitrobot Mark IV (Thermo Fisher, Altrincham, UK), followed by a second incubation of 2 mins. Final concentrations of proteins were: 0.125 µM actin, 2.5 µM Myo5a-S1, 5 µM CaM. All dilutions were done in 100 mM KCl, 0.1 mM EGTA, 1 mM $MgCl_2$, 10 mM MOPS, pH 7.0. Grids were then blotted with Whatman no. 42 Ashless filter paper (Agar Scientific, Stansted, UK) for 3 s at force -25, 8 °C and 80 % humidity, drained for 0.5 s and flash-frozen in liquid ethane. Data was recorded on the FEI Titan Krios I (Astbury Biostructure Laboratory, University of Leeds, Leeds, UK) equipped with a FEI Falcon III detector operating in linear mode (**Error! Reference source not found.**).

Cryo-EM image processing

First, MotionCor2 (Zheng et al., 2017) was used to correct for beam-induced motion, and the contrast transfer function (CTF) was estimated using Gctf (GPU accelerated CTF) (Zhang, 2016), before subsequent processing steps (Figure 7). The start-end coordinates of F-actin filaments were manually picked using RELION 3.1 (Zivanov et al., 2018). Particles were extracted in RELION 3.1 using helical parameters (box size 608 px, helical rise 27.5 Å, tube diameter 250 Å). The data was initially binned 2 x to 2.13 Å. Helical 3D refinement was used to produce an initial model (tube outer diameter 140 Å, angular search range tilt 15° and psi 10°, initial twist -166.15°, helical rise 27.5 Å, twist search -165° to -167° with a 0.1° step, rise search 26.5° to 28.5° with a 0.1° step). A known structure of the Myo5a motor (PDB: 7PLU, (Pospich et al., 2021)) was rigid fit into the helical refinement map at a motor domain that was the most well resolved and positioned at the centre of the box, using Chimera (Pettersen et al., 2004). A map of the fitted PDB structure was generated in Chimera

(Pettersen et al., 2004), and used as input to generate a wide mask of the motor domain in RELION 3.1 for masked 3D classification (Zivanov et al., 2018). Masked 3D classification was performed in RELION 3.1 to classify out undecorated actin and to only include particles with myosin bound at the centre of the box (5 classes, no image alignment, regularisation parameter T = 4). This dataset was then un-binned (1.065 Å) as initial reconstructions were reaching the Nyquist limit. 3D helical refinement followed by masked post-processing of this subset of particles produced a map with a 3.8 Å global resolution, but with limited detail across the lever. All global resolutions were determined using the gold standard Fourier Shell Correlation (FSC) reported to FSC = 0.143 using RELION 3.1. To compare the motor domain to the previously published chicken actomyosin-5a rigor structure (PDB: 7PLU (Pospich et al., 2021)), particle subtraction was performed subtracting all density outside of a mask comprising of the motor, the first 2 CaMs and 3 F-actin subunits (2IQ). 3D refinement followed by post-processing, produced a map with a global resolution of 4.2 Å according to the $FSC_{0.143}$-criterion, which was highly similar to that previously published (3.2 Å, PDB: 7PLU (Pospich et al., 2021)). The 2IQ map was locally sharpened using DeepEMhancer (Sanchez-Garcia et al., 2021).

To improve lever resolution, particle subtraction was required to aid particle alignment and centralise the lever domain within the box. It was noted from initial 3D helical reconstructions that there was smearing of the lever density, so a wide mask containing 1 actin subunit, the motor and a cone shape for the lever to accommodate flexibility was used for subtraction (Figure 7). A map was generated in Chimera comprising of a single actin subunit, a motor (both from PDB: 7PLU, (Pospich et al., 2021)), and multiple copies of a Myo5a lever model (PDB: 2DFS (Liu et al., 2006)) arranged in a cone shape tapering at the motor and splaying towards the lever end. These were positioned so that the boundaries of the cone met the density of the neighbouring actin bound heads in the helical map. A wide cone-shaped mask was generated in RELION 3.1 using the cone-shaped map. Signal outside of this mask was subtracted from the binned (to 2.13 Å) 2D images, and particles were re-centred bringing the lever to the focal point of the box. 3D refinement of the subtracted particles produced a map (cone subtracted map) with 4.3 Å global resolution according to the $FSC_{0.143}$-criterion. This map was locally sharpened using DeepEMhancer (Sanchez-Garcia et al., 2021). The cone subtracted map had improved resolution across the lever, however defined density for CaMs 5 and 6 could not be seen (Figure 7).

In order to resolve CaMs 5 and 6, 3D classification of the lever domain using a cone shaped lever mask was performed. This mask was generated in the same was as previously, but excluding the actin subunit and motor domain in order to classify based on lever conformation only. Classification into 10 or 20 classes both produced ~9 reasonable classes. However, the conformations reconstructed by 3D classification were not distinct conformational states but continuous thermally driven motion, as the conformation of the classes produced differed in both modes of division (10 or 20). The significance of 9 classes is instead likely to be the number of groups the particles could be reasonably divided into to have sufficient particles to produce a reconstruction. The maps were locally sharpened using DeepEMhancer (Sanchez-Garcia et al., 2021). Though classification led to a reduction in overall resolution due to loss of particles in the reconstruction, for the first time we are able to see across the full length of the lever while the motor is actin bound (Figure 7).

However, we cannot rule out that there may be particles representing more extreme lever conformations outside of the subtraction and classification masks used to focus the image processing.

The cryo-EM 3D class with the best global resolution (7.5 Å) was selected to build a pseudoatomic lever model. The local resolution of this map was calculated using SPOC (statistical post-processing of cryo-EM maps), as the local resolution calculations in RELION are unreliable at resolutions lower than 10 Å (Beckers and Sachse, 2020).

Cryo-EM model building and refinement

An initial lever model including the converter + 6IQ motifs sequence (698-907) + 8 residue FLAG-tag, and 6 CaM sequences, was built in Alphafold 2.0 using collabfold Google collab notebooks (Mirdita et al., 2022). This model was then flexibly fit into the density of the best 3D class using Isolde (Croll, 2018), applying distance and torsional restraints taken from murine IQ1-2 and CaM1-CaM2 structure (PDB: 2IX7, (Houdusse et al., 2006)) to each CaM pair. Distance and torsional restraints from the Myo2p 25-residue spaced pair structure (PDB: 1N2D, (Terrak et al., 2005)) were applied to interacting residues in 25-residue spaced pairs (Glu14-Arg91, in CaM2-3 and CaM4-5), as density corresponding to these interactions could be seen in the selected class map. Only the C-lobe of CaM6 was included in fitting as only density for this half of the molecule could be seen in the map. To model the N-lobe of CaM6 a homology model of CaM in an extended state, based on a Myo2p-MLC1P structure (PDB: 1M46, (Terrak et al., 2003)), was built using Swiss-model (Waterhouse et al., 2018). The C-lobe of the homology model was superimposed onto the C-lobe of the initial CaM6 model. The N-lobe (residues 3-84) of the homology model was then joined to the C-lobe of the initial CaM6 model, and minimised in Isolde without map weighting.

A pseudoatomic lever model was generated by performing all-atom MD simulations of the fitted lever model to gain side-chain conformations. All simulations were performed using Amber20 (Case et al., 2020) with the FF19SB forcefield (Tian et al., 2020). The lever model was protonated according to the Amber residue templates and then solvated with TIP3P water molecules in an octahedral box that extended 14 Å from the protein. K^+ ions were added to neutralise the system, then KCl was added to a final concentration of 100 mM. After initial energy minimisation the system was heated to 300 K as positional restraints were decreased from 100 to 0 kcal/mol/Å^2, except for across the lever heavy chain. A restraint of 1 kcal/mol/Å^2 was applied to the backbone of the lever heavy chain throughout the minimisation, equilibration and production runs, to permit CaM motion and interaction with the heavy chain side-chains, but maintain the lever position seen in the cryo-EM map. Minimisation and equilibration steps were performed on the ARC4 standard nodes (Intel Xeon Gold 6138 CPUs ('Sky Lake')). NMR distance restraints were also applied between interactions visible in the cryo-EM density (Glu14-Arg90). To do this, distance restraints were applied between the Cδ atom of Glu, and Cζ of Arg, in order not to dictate which N and O interact. These were weighted at 20 kcal/mol/Å^2 within 1.9 Å of the bounds of the flat well restraint (3.4-5.3 Å), and a 20 kcal/mol/Å^2 harmonic potential was applied outside of this range. The MD production runs used the pmemd.cuda module from Amber20 and were run on Bede

using Tesla V100 GPUs. MD was performed for 300 ns in triplicate repeat. The Berendsen Thermostat was used as recommended to maximise GPU performance.

Following simulation, the average conformation was calculated in VMD (Visual Molecular Dynamics) (Humphrey et al., 1996), and the frame of the trajectory with the lowest global RMSD (Root Mean Square Deviation) with the average conformation was selected as a model for each repeat. A further round of minimisation was then performed on the ARC4 general nodes to restore side-chains to low energy conformations. After minimisation, each model was scored in MolProbity (Chen et al., 2009), and the repeat with the lowest MolProbity score and the largest proportion within the cryo-EM density was selected as the final lever model.

To compare the flexibility of each CaM, per residue root mean square fluctuation (RMSF) analysis was performed using CPPTRAJ on each CaM in the restrained simulation and for each repeat (Roe and Cheatham, 2013).

Unrestrained MD simulations were run in conjunction with the restrained simulations to compare the contacts found in both. Unrestrained MD simulations were performed under the same conditions as previously, however without restraints applied. The timescale for the overall motion of the lever can be estimated from Equation (**1**) by equating the viscous drag force on the lever in explicit water to the overall cantilever stiffness,

$$\text{timescale of motion} = \frac{\mu L}{k_{cantilever}}, \qquad \textbf{(1)}$$

where μ = 1 pN nm^{-2} ns (the viscosity of water), L = 20 nm (approximate lever length), k_{ove} = 0.76 pN/nm (lever overall cantilever bending stiffness). This gives a relaxation timescale of ~15 ns. Therefore, a 300 ns simulation should contain ~20 independent observations of the slowest motion. Although ~1000 observations would be required for robust statistical analysis, ~20 independent observations in triplicate repeat should be sufficient to identify prevalent interactions.

To generate a model of the motor domain, a homology model of murine Myo5a was made using the chicken actomyosin-5a rigor structure (PDB:7PLU, (Pospich et al., 2021)) as the template in Swiss-model (Waterhouse et al., 2018). This was then fit into the cryo-EM density using Isolde (Croll, 2018), applying distance and torsional restraints based on the template. Residues 1-698 where then joined to the pseudoatomic lever model (699-915). The regularize zone tool in Coot was used to correct over the stitch region (Emsley et al., 2010). The F-actin subunits from the chicken actomyosin-5a rigor structure (PDB:7PLU, (Pospich et al., 2021)), with phalloidin removed, were also fit into the density corresponding to actin using Isolde (Croll, 2018). As the resolution of F-actin and the motor domain was insufficient to fit side-chains, and their structures have already been published at high-resolution, only the backbone is included for these domains in our model (Pospich et al., 2021). Side-chain orientations are included for the lever from the simulated data. The quality of the final model was assessed using MolProbity (Chen et al., 2009) (Table 3).

Flexibility analysis

To calculate angles and distances between lever subdomains, the Isolde generated lever model (pre-simulation) and the homology model of the motor were flexibly fit into each cryo-EM class with torsional and distance restraints applied using Isolde (Croll, 2018). To calculate the angles, the molecule was subdivided into 7 mobile domains: base (actin binding interface), converter, and CaMs 1-6 (Figure 4 Supplement 1A). Vectors were used to represent each domain, drawn between Cα atoms for the base (res 384 and 543), the converter (res 721 and 760), and CaMs (res 136 and 63). Local material axes uvw were calculated for each subdomain pair. The u axis is the vector between the midpoints of each vector in the subdomain pair. The v axis is the vector that is orthogonal to u, and a 45° rotation about u from the vector presenting the first subdomain of the pair. The w axis is the vector orthogonal to u and v, so that the vector representing the first subdomain of the pair lies halfway between v and -w. The angles between the subdomain vector pairs were then calculated in each plane (vw, uv and uw). $\theta_{vw} = \theta$, $\theta_{uv} = \theta_1 - \theta_2$, $\theta_{uw} = \theta_3 - \theta_4$ (Figure 4 Supplement 1C-E). Distances were calculated between the Cα atoms of known interacting residues in the N- and C-lobe of consecutive CaMs (Ser17 and Asn111, respectively).

To calculate the spring constants at the connections between lever subdomains (k_{sub}), the variance (σ^2) in angle between subdomain pairs within the classes (weighted by the number of particles in each class), was calculated in 3 orthogonal planes (vw, uv, uw) (Figure 1 supplement 1 and Figure 4 supplement 1). The vw plane describes torsional stiffness, and the uv and uw plane describe bending stiffness in 2 directions (Figure 4 supplement 1). k_{sub} in each plane was calculated using Equation (**2**),

$$\text{spring constant } (\mathrm{k_{sub}}) = \frac{k_B T}{\sigma^2}, \qquad \textbf{(2)}$$

where $k_B = 1.38 \times 10^{-23}$ N m K^{-1} (Boltzmann constant), T = 281.15 K (temperature of grid making in Kelvin), and σ^2 is the variance in angle between subdomain pairs within the classes. The overall bending stiffness was calculated by averaging the values in the uv and uw plane.

The error for the bending stiffness calculation at each subdomain was estimated from the standard deviation (SD) of bending stiffnesses calculated by randomly varying angles between the subdomains within reasonable bounds, given the grouping of molecules into classes. For each subdomain pair, the angles calculated between the subdomain pair in each class were sorted into ascending order. A new value for this angle was generated for each class, chosen randomly between the angle values either side of it in the sorted list. The ranges for values at the start and end of the list were calculated using the value ± the distance from the single neighbour. The variance (σ^2) was calculated for these randomly assigned angles, and used to calculate a bending stiffness using Equation (**2**). This process was repeated 1000 times, generating a new estimate of the spring constant each time. The SD of these randomly obtained bending stiffnesses was quoted as the error.

To calculate the cantilever bending stiffness of the whole lever, a vector representing the lever was drawn between the midpoint of the vector describing the converter, and the midpoint of the vector describing CaM6 for all classes (Figure 4 supplement 1). The mean of the lever vectors was calculated. To determine the variance in lever displacement, a new coordinate system was calculated using the mean vector as the z-axis (Figure 5C-D). The y-axis was calculated as the vector that is orthogonal to z, which sits in the plane of z and the vector representing F-actin (res 145 of the 1st and 13th subunit of a model F-actin). The model of F-actin was made by superimposing the first and last subunit of multiple copies of the actin from 7PLU (Pospich et al., 2021). The x-axis was calculated as the vector orthogonal to z and y. The distance between the end point of the lever unit vector and the end point of the mean unit vector was calculated for each class (d_c) in xy (Figure 8). The variance in lever conformation was calculated using Equation (**3**),

$$\text{lever variance} = \frac{\sum_{c=1}^{a} n_c d_c^2}{\sum_{c=1}^{a} n_c}, \qquad \textbf{(3)}$$

where n_c is the number of particles in the class, and d_c is distance between the class unit vector and the mean unit vector. This was done for the overall displacement (Figure 8A-B) and also for displacement in a particular direction (tilt/slew) (Figure 8A & C), to calculate the overall bending stiffness and the bending stiffness in both directions (tilt/slew).

The overall cantilever bending stiffness (k_{ov}) was calculated using Equation (**4**),

$$\mathrm{k}_{ov} = \frac{2k_B T}{{\sigma_{3D}}^2 L^2}, \qquad \textbf{(4)}$$

where k_B = 1.38 x 10^{-23} N m K^{-1} (Boltzmann constant), T = 281.15 K (temperature of grid making in Kelvin), L is the mean length of the lever vectors, and σ_{3D}^2 is the variance calculated from the overall displacement within the 2 degrees of freedom. A factor of 2 is included in Equation (**4**) to account for the two degrees of freedom in bending along two perpendicular directions.

The directional cantilever bending stiffness (k_{dir}) was calculated using Equation **(5)**,

$$\mathrm{k}_{dir} = \frac{k_B T}{{\sigma_i}^2 L^2}, \qquad \textbf{(5)}$$

where k_B = 1.38 x 10^{-23} N m K^{-1} (Boltzmann constant), T = 281.15 K (temperature of grid making in Kelvin), L is the mean length of the lever vectors, and σ_i^2 is the variance calculated from the displacement in a particular direction (x or y).

The error for the cantilever bending stiffness calculations was estimated from the standard deviation (SD) of bending stiffnesses calculated by randomly varying the value for displacement of the lever from the mean within reasonable bounds, given the grouping of molecules into classes. The values for displacement from the mean of each class were sorted into ascending order. A new value for this displacement was generated for each class, chosen randomly between the displacement values

either side of it in the sorted list. The ranges for values at the start and end of the list were calculated using the value ± the distance from the single neighbour. The randomly generated displacements were used to calculate the unweighted variance using Equation **(6)**,

$$\text{lever variance} = \frac{\sum_{c=1}^{a} d_c^2}{9}, \qquad \textbf{(6)}$$

where d_c is the randomly generated displacement. This variance was used to calculate the cantilever bending stiffness using Equation **(4)** for the overall bending stiffness and Equation **(5)** for the directional bending stiffness in each direction. This process was repeated 1000 times, generating a new estimate of the cantilever bending stiffness each time. The SD of these randomly obtained bending stiffnesses was quoted as the error.

Predicting the working stroke

The ensemble of lever conformations in the cryo-EM 3D classes were used to predict the working stroke of Myo5a-S1. To determine the distance the working stroke translates the end of the lever along F-actin longitudinal axis, a vector between the 1st and 13th subunit (Cα, residue 145) of F-actin was calculated from an F-actin model. The F-actin model was produced by superimposing multiple copies of the first and last subunit of actin in the rigor actomyosin-5a model (PDB: 7PLU (Pospich et al., 2021)) (as above). The lever models generated from each cryo-EM class were superimposed onto the converter of a pre-powerstroke (PDB: 4ZG4, (Wulf et al., 2016)), and post-powerstroke structure (PDB: 7PM6, (Pospich et al., 2021)). As 4ZG4 is not actin bound, to model the motor bound in the ADP-P_i (pre-powestroke) state the L50 domain of 4ZG4 was superimposed with the actin interacting region of the L50 domain of 7PM6, as the L50 domain is thought to bind actin first (Holmes et al., 2003). A vector between the lever end (res 914) of each class model of the ADP-P_i state to every other class model of the ADP state was drawn. The magnitude of this vector projected onto the vector defining F-actin was then used to determine the translation of the lever end along F-actin. The probability of a combination of classes being paired was calculated by taking the probability of an individual class occurring, using the fraction of particles in each class out of the total number of particles. The probabilities of each class in a pair were multiplied to give the probability of that combination of classes being paired.

Acknowledgements

We would like to thank Eva Forgacs, Betty Virok and Howard White for the generous gift that was the purified Myo5a-S1 protein. We would like to thank Glenn Carrington, Peter J. Knight and Yasuharu Takagi for the helpful discussion and advice. We would like to thank the Astbury Biostructure Laboratory for their support. The FEI Titan Krios microscopes were funded by the University of Leeds (UoL ABSL award) and Wellcome Trust (108466/Z/15/Z). This work made use of the facilities of the N8 Centre of Excellence in Computationally Intensive Research (N8 CIR) provided and funded by the N8 research partnership and EPSRC (EP/T022167/1), through HECBioSim (EP/R013012). The Centre is co-ordinated by the Universities of Durham, Manchester and York, UK. This work was also undertaken on ARC4, part of

the High Performance Computing facilities at the University of Leeds, UK. Molly S. C. Gravett and David P. Klebl were PhD students on the Wellcome Trust 4-year PhD program (102174/B/13/Z) in The Astbury Centre funded by The University of Leeds. Michelle Peckham is funded by the Wellcome Trust Investigator award 'Myosin structure and regulation' (223125/Z/21/Z).

References

Alves, C.P., Moraes, M.H., Sousa, J.F., Pontes, C.L.S., Ramão, A., Yokoyama, S., Trindade, D.M., Fisher, D.E. and Espreafico, E.M. 2013. Myosin-Va contributes to manifestation of malignant-related properties in melanoma cells. *Journal of Investigative Dermatology*. **133**(12), pp.2809–2812.

Andrecka, J., Ortega Arroyo, J., Takagi, Y., de Wit, G., Fineberg, A., MacKinnon, L., Young, G., Sellers, J.R. and Kukura, P. 2015. Structural dynamics of myosin 5 during processive motion revealed by interferometric scattering microscopy. *eLife*. **4**, p.e05413.

Baboolal, T.G., Sakamoto, T., Forgacs, E., White, H.D., Jackson, S.M., Takagi, Y., Farrow, R.E., Molloy, D.E., Knight, P.J., Sellers, J.R. and Peckhama, M. 2009. The SAH domain extends the functional length of the myosin lever. *Proceedings of the National Academy of Sciences of the United States of America*. **106**(52), pp.22193–22198.

Bähler, M. and Rhoads, A. 2002. Calmodulin signaling via the IQ motif. *FEBS Letters*. **513**(1), pp.107–113.

Beckers, M. and Sachse, C. 2020. Permutation testing of Fourier shell correlation for resolution estimation of cryo-EM maps. *Journal of Structural Biology*. **212**(1), p.107579.

Billington, N., Revill, D.J., Burgess, S.A., Chantler, P.D. and Knight, P.J. 2014. Flexibility within the Heads of Muscle Myosin-2 Molecules. *Journal of Molecular Biology*. **426**(4), pp.894–907.

Black, D.J. and Persechini, A. 2010. Variations at the semiconserved glycine in the IQ domain consensus sequence have a major impact on Ca2+-dependent switching in calmodulin-IQ domain complexes. *Biochemistry*. **49**(1), pp.78–83.

Burgess, S., Walker, M., Wang, F., Sellers, J.P., White, H.D., Knight, P.J. and Trinick, J. 2002. The prepower stroke conformation of myosin V. *Journal of Cell Biology*. **159**(6), pp.983–991.

Case, D.A., Aktulga, H.M., Belfon, K., Ben-Shalom, I.Y., Berryman, J.T., Brozell, S.R., Cerutti, D.S., Cheatham, T.E., I., Cisneros, G.A., Cruzeiro, V.W.D., Darden, T.A., Duke, R.E., Giambasu, G., Gilson, M.K., Gohlke, H., Goetz, A.W., Harris, R., Izadi, S., Izmailov, S.A. and Kollman, P.A. 2020. Amber 2020.

Chen, V.B., Arendall, W.B., Headd, J.J., Keedy, D.A., Immormino, R.M., Kapral, G.J., Murray, L.W., Richardson, J.S. and Richardson, D.C. 2009. MolProbity: all-atom structure validation for macromolecular crystallography. *urn:issn:0907-*

4449. **66**(1), pp.12–21.

Croll, T.I. 2018. ISOLDE: A physically realistic environment for model building into low-resolution electron-density maps. *Acta Crystallographica Section D: Structural Biology*. **74**(6), pp.519–530.

Emsley, P., Lohkamp, B., Scott, W.G. and Cowtan, K. 2010. Features and development of Coot. *urn:issn:0907-4449*. **66**(4), pp.486–501.

Forgacs, E., Cartwright, S., Kovács, M., Sakamoto, T., Sellers, J.R., Corrie, J.E.T., Webb, M.R. and White, H.D. 2006. Kinetic mechanism of myosin V-SI using a new fluorescent ATP analogue. *Biochemistry*. **45**(43), pp.13035–13045.

Forgacs, E., Cartwright, S., Sakamoto, T., Sellers, J.R., Corrie, J.E.T., Webb, M.R. and White, H.D. 2008. Kinetics of ADP dissociation from the trail and lead heads of actomyosin V following the power stroke. *Journal of Biological Chemistry*. **283**(2), pp.766–773.

Foth, B.J., Goedecke, M.C. and Soldati, D. 2006. New insights into myosin evolution and classification. *Proceedings of the National Academy of Sciences of the United States of America*. **103**(10), pp.3681–3686.

Van Gele, M., Dynoodt, P. and Lambert, J. 2009. Griscelli syndrome: a model system to study vesicular trafficking. *Pigment Cell & Melanoma Research*. **22**(3), pp.268–282.

Hammer, J.A. and Sellers, J.R. 2012. Walking to work: Roles for class v myosins as cargo transporters. *Nature Reviews Molecular Cell Biology*. **13**(1), pp.13–26.

Hartman, M.A. and Spudich, J.A. 2012. The myosin superfamily at a glance. *Journal of Cell Science*. **125**(7), pp.1627–1632.

Heissler, S.M. and Sellers, J.R. 2015. Myosin light chains: Teaching old dogs new tricks. *Ceased*. **4**(6), pp.169–188.

Holmes, K.C., Angert, I., Kull, F.J., Jahn, W. and Schröder, R.R. 2003. Electron cryo-microscopy shows how strong binding of myosin to actin releases nucleotide. *Nature 2003 425:6956*. **425**(6956), pp.423–427.

Houdusse, A., Gaucher, J.F., Krementsova, E., Mui, S., Trybus, K.M. and Cohen, C. 2006. Crystal structure of apo-calmodulin bound to the first two IQ motifs of myosin V reveals essential recognition features. *Proceedings of the National Academy of Sciences of the United States of America*. **103**(51), pp.19326–19331.

Houdusse, A., Szent-Györgyi, A.G. and Cohen, C. 2000. Three conformational states of scallop myosin S1. *Proceedings of the National Academy of Sciences of the United States of America*. **97**(21), pp.11238–11243.

Humphrey, W., Dalke, A. and Schulten, K. 1996. VMD: Visual molecular dynamics. *Journal of Molecular Graphics*. **14**(1), pp.33–38.

Kollmar, M. and Mühlhausen, S. 2017. Myosin repertoire expansion coincides with eukaryotic diversification in the Mesoproterozoic era. *BMC Evolutionary Biology*. **17**(1), pp.1–18.

De La Cruz, E.M. and Ostap, E.M. 2004. Relating biochemistry and function in the myosin superfamily. *Current Opinion in Cell Biology*. **16**(1), pp.61–67.

Lan, L., Han, H., Zuo, H., Chen, Z., Du, Y., Zhao, W., Gu, J. and Zhang, Z. 2010. Upregulation of myosin Va by Snail is involved in cancer cell migration and metastasis. *International Journal of Cancer*. **126**(1), pp.53–64.

Liu, J., Taylor, D.W., Krementsova, E.B., Trybus, K.M. and Taylor, K.A. 2006. Three-dimensional structure of the myosin V inhibited state by cryoelectron tomography. *Nature*. **442**(7099), pp.208–211.

Lombardo, A.T., Nelson, S.R., Kennedy, G.G., Trybus, K.M., Walcott, S. and Warshaw, D.M. 2019. Myosin Va transport of liposomes in three-dimensional actin networks is modulated by actin filament density, position, and polarity. *Proceedings of the National Academy of Sciences of the United States of America*. **116**(17), pp.8326–8335.

Mercer, J.A., Seperack, P.K., Strobel, M.C., Copeland, N.G. and Jenkins, N.A. 1991. Novel myosin heavy chain encoded by murine dilute coat colour locus. *Nature*. **349**(6311), pp.709–713.

Mirdita, M., Schütze, K., Moriwaki, Y., Heo, L., Ovchinnikov, S. and Steinegger, M. 2022. ColabFold: making protein folding accessible to all. *Nature Methods 2022 19:6*. **19**(6), pp.679–682.

Niu, F., Liu, Y., Sun, K., Xu, S., Dong, J., Yu, C., Yan, K. and Wei, Z. 2022. Autoinhibition and activation mechanisms revealed by the triangular-shaped structure of myosin Va. *Science Advances*. **8**(49).

Oke, O.A., Burgess, S.A., Forgacs, E., Knight, P.J., Sakamoto, T., Sellers, J.R., White, H. and Trinick, J. 2010. Influence of lever structure on myosin 5a walking. *Proceedings of the National Academy of Sciences of the United States of America*. **107**(6), pp.2509–2514.

Pardee, J.D. and Spudich, J.A. 1982. Chapter 18 Purification of Muscle Actin. *Methods in Cell Biology*. **24**(C), pp.271–289.

Pastural, E., Barrat, F.J., Dufourcq-Lagelouse, R., Certain, S., Sanal, O., Jabado, N., Seger, R., Griscelli, C., Fischer, A. and De Saint Basile, G. 1997. Griscelli disease maps to chromosome 15q21 and is associated with mutations in the myosin-Va gene. *Nature Genetics*. **16**(3), pp.289–292.

Pettersen, E.F., Goddard, T.D., Huang, C.C., Couch, G.S., Greenblatt, D.M., Meng, E.C. and Ferrin, T.E. 2004. UCSF Chimera - A visualization system for exploratory research and analysis. *Journal of Computational Chemistry*. **25**(13), pp.1605–1612.

Pettersen, E.F., Goddard, T.D., Huang, C.C., Meng, E.C., Couch, G.S., Croll, T.I.,

Morris, J.H. and Ferrin, T.E. 2021. UCSF ChimeraX: Structure visualization for researchers, educators, and developers. *Protein Science*. **30**(1), pp.70–82.

Pospich, S., Sweeney, H.L., Houdusse, A. and Raunser, S. 2021. High-resolution structures of the actomyosin-v complex in three nucleotide states provide insights into the force generation mechanism. *eLife*. **10**, p.e73724.

Provance, D.W. and Mercer, J.A. 1999. Myosin-V: Head to tail. *Cellular and Molecular Life Sciences*. **56**(3–4), pp.233–242.

Reck-Peterson, S.L., Provance, D.W., Mooseker, M.S. and Mercer, J.A. 2000. Class V myosins. *Biochimica et Biophysica Acta - Molecular Cell Research*. **1496**(1), pp.36–51.

Roe, D.R. and Cheatham, T.E. 2013. PTRAJ and CPPTRAJ: Software for processing and analysis of molecular dynamics trajectory data. *Journal of Chemical Theory and Computation*. **9**(7), pp.3084–3095.

Sakamoto, T., Wang, F., Schmitz, S., Xu, Y., Xu, Q., Molloy, J.E., Veigel, C. and Sellers, J.R. 2003. Neck length and processivity of myosin V. *Journal of Biological Chemistry*. **278**(31), pp.29201–29207.

Sanchez-Garcia, R., Gomez-Blanco, J., Cuervo, A., Carazo, J.M., Sorzano, C.O.S. and Vargas, J. 2021. DeepEMhancer: a deep learning solution for cryo-EM volume post-processing. *Communications Biology 2021 4:1*. **4**(1), pp.1–8.

Sivaramakrishnan, S., Spink, B.J., Sim, A.Y.L., Doniach, S. and Spudich, J.A. 2008. Dynamic charge interactions create surprising rigidity in the ER/K α-helical protein motif. *Proceedings of the National Academy of Sciences of the United States of America*. **105**(36), pp.13356–13361.

Terrak, M., Rebowski, G., Lu, R.C., Grabarek, Z. and Dominguez, R. 2005. Structure of the light chain-binding domain of myosin V. . **6**(36).

Terrak, M., Wu, G., Stafford, W.F., Lu, R.C. and Dominguez, R. 2003. Two distinct myosin light chain structures are induced by specific variations within the bound IQ motifs—functional implications. *The EMBO Journal*. **22**(3), pp.362–371.

Tian, C., Kasavajhala, K., Belfon, K.A.A., Raguette, L., Huang, H., Migues, A.N., Bickel, J., Wang, Y., Pincay, J., Wu, Q. and Simmerling, C. 2020. Ff19SB: Amino-Acid-Specific Protein Backbone Parameters Trained against Quantum Mechanics Energy Surfaces in Solution. *Journal of Chemical Theory and Computation*. **16**(1), pp.528–552.

Titus, M.A. 2018. Myosin-driven intracellular transport. *Cold Spring Harbor Perspectives in Biology*. **10**(3).

Veigel, C., Wang, F., Bartoo, M.L., Sellers, J.R. and Molloy, J.E. 2002. The gated gait of the processive molecular motor, myosin V. *Nature Cell Biology*. **4**(1), pp.59–65.

Wagner, W., Brenowitz, S.D. and Hammer, J.A. 2011. Myosin-Va transports the

endoplasmic reticulum into the dendritic spines of Purkinje neurons. *Nature Cell Biology*. **13**(1), pp.40–47.

Walker, M.L., Burgess, S.A., Sellers, J.R., Wang, F., Hammer, J.A., Trinick, J. and Knight, P.J. 2000. Two-headed binding of a processive myosin to F-actin. *Nature*. **405**(6788), pp.804–807.

Wang, F., Chen, L., Arcucci, O., Harvey, E. V., Bowers, B., Xu, Y., Hammer, J.A. and Sellers, J.R. 2000. Effect of ADP and ionic strength on the kinetic and motile properties of recombinant mouse myosin V. *Journal of Biological Chemistry*. **275**(6), pp.4329–4335.

Waterhouse, A., Bertoni, M., Bienert, S., Studer, G., Tauriello, G., Gumienny, R., Heer, F.T., de Beer, T.A.P., Rempfer, C., Bordoli, L., Lepore, R. and Schwede, T. 2018. SWISS-MODEL: homology modelling of protein structures and complexes. *Nucleic Acids Research*. **46**(W1), pp.W296–W303.

Wulf, S.F., Ropars, V., Fujita-Becker, S., Oster, M., Hofhaus, G., Trabuco, L.G., Pylypenko, O., Sweeney, H.L., Houdusse, A.M., Schröder, R.R. and Vale, R.D. 2016. Force-producing ADP state of myosin bound to actin. *Proceedings of the National Academy of Sciences of the United States of America*. **113**(13), pp.E1844–E1852.

Zhang, K. 2016. Gctf: Real-time CTF determination and correction. *Journal of Structural Biology*. **193**(1), pp.1–12.

Zheng, S.Q., Palovcak, E., Armache, J.-P., Verba, K.A., Cheng, Y. and Agard, D.A. 2017. MotionCor2: anisotropic correction of beam-induced motion for improved cryo-electron microscopy. *Nature Methods*. **14**(4), pp.331–332.

Zivanov, J., Nakane, T., Forsberg, B.O., Kimanius, D., Hagen, W.J., Lindahl, E. and Scheres, S.H. 2018. New tools for automated high-resolution cryo-EM structure determination in RELION-3. *eLife*. **7**, p.e42166.

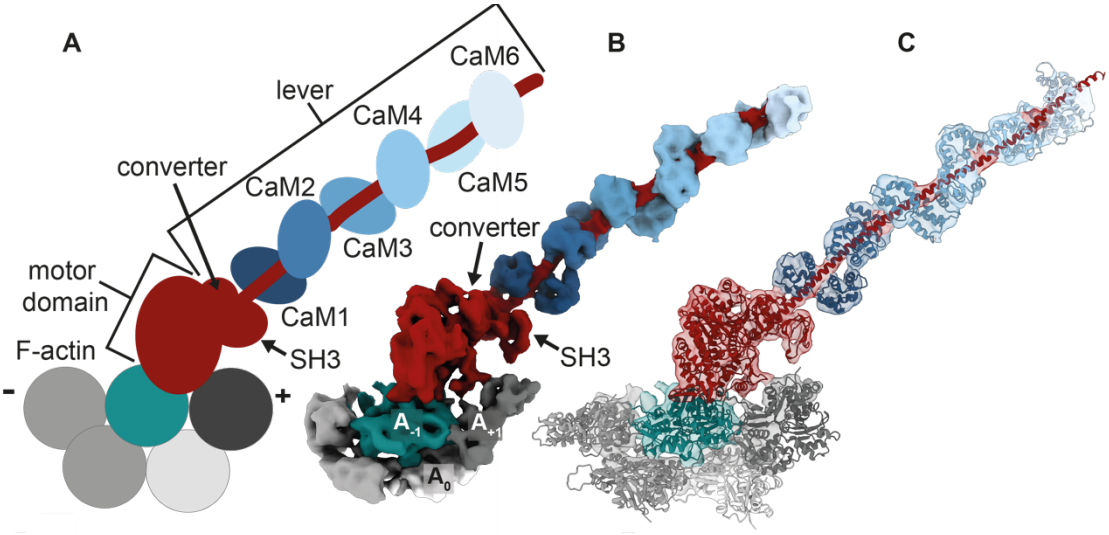

Figure 1: Structure of Myo5a-S1-6IQ bound to actin

A: *Schematic of Myo5a-S1 bound to filamentous actin (F-actin). The motor domain is shown in red, with the position of its N-terminal SH3-like fold domain and C-terminal converter domain indicated. The lever is comprised of 6 IQ motifs bound to calmodulin (CaM). CaMs are labelled CaM 1-6, where the number refers to which IQ motif the CaM is bound to. The polarity of F-actin is indicated by + for the plus and – for the minus end of the filament. The two adjacent actin subunits that interact with the motor domain are coloured green for the actin subunit closest to the minus end* A_{-1}*, and dark grey for the actin subunit closest to the plus end* A_{+1}*.* ***B:*** *Cryo-EM split map (contour level: 0.25) of a single Myo5a-S1-6IQ class with the full-length lever (global resolution of 7.5 Å at 0.143 FSC).* ***C:*** *The cryo-EM density map (contour level: 0.25) of Myo5a-S1-6IQ fit with the pseudoatomic model.*

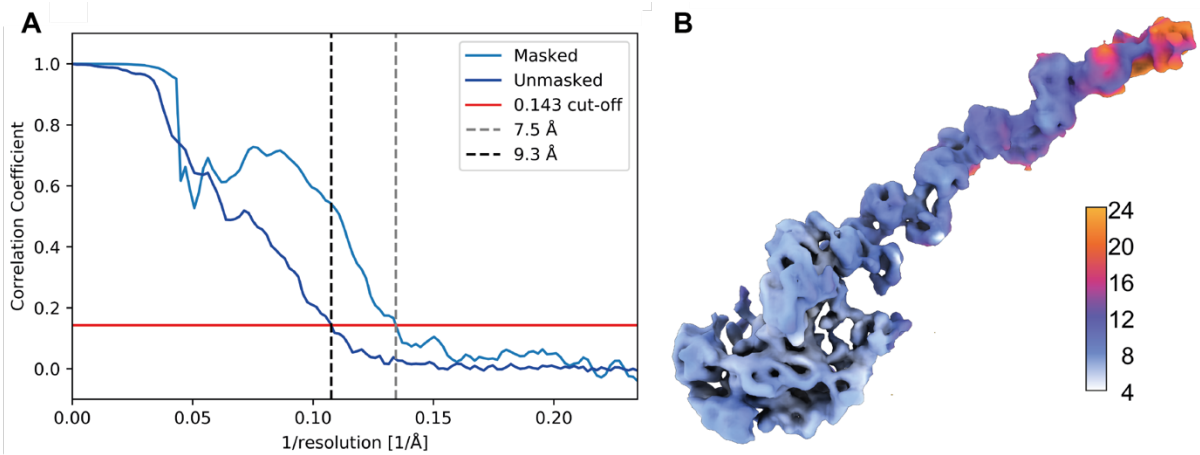

Figure 1 – supplement 1: cryo-EM map resolution.

A: *Fourier shell correlation (FSC) curve illustrating masked 7.5 Å resolution and unmasked 9.3 Å resolution at 0.143 FSC.* ***B:*** *Local resolution calculated with SPOC (Statistical Processing of Cryo-EM maps) (Beckers and Sachse, 2020) displayed on the actin bound Myo5a-S1-6IQ cryo-EM map (contour level: 0.25). Colour bar shows the resolution in Å.*

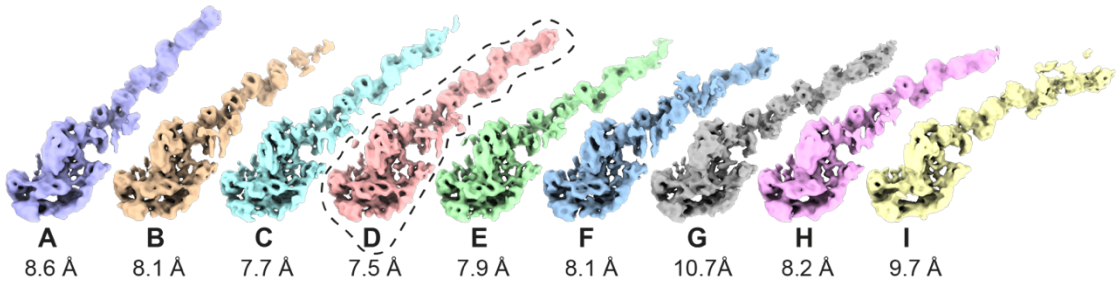

Figure 1 – supplement 2: 9 sub-classes of Myo5a-S1-6IQ bound to F-actin following 3D classification

Images ***A-I*** *show cryo-EM maps for each 3D class, post-processed using DeepEMhancer (Sanchez-Garcia et al., 2021), and with dust hidden (contour level: 0.28). The estimate of the masked global resolution at 0.143 FSC (Fourier Shell Correlation) is displayed beneath each class. The circled class (****D****) shows the class with the best resolution that was selected for model building (displayed in the main figure (Figure 1B-C)).*

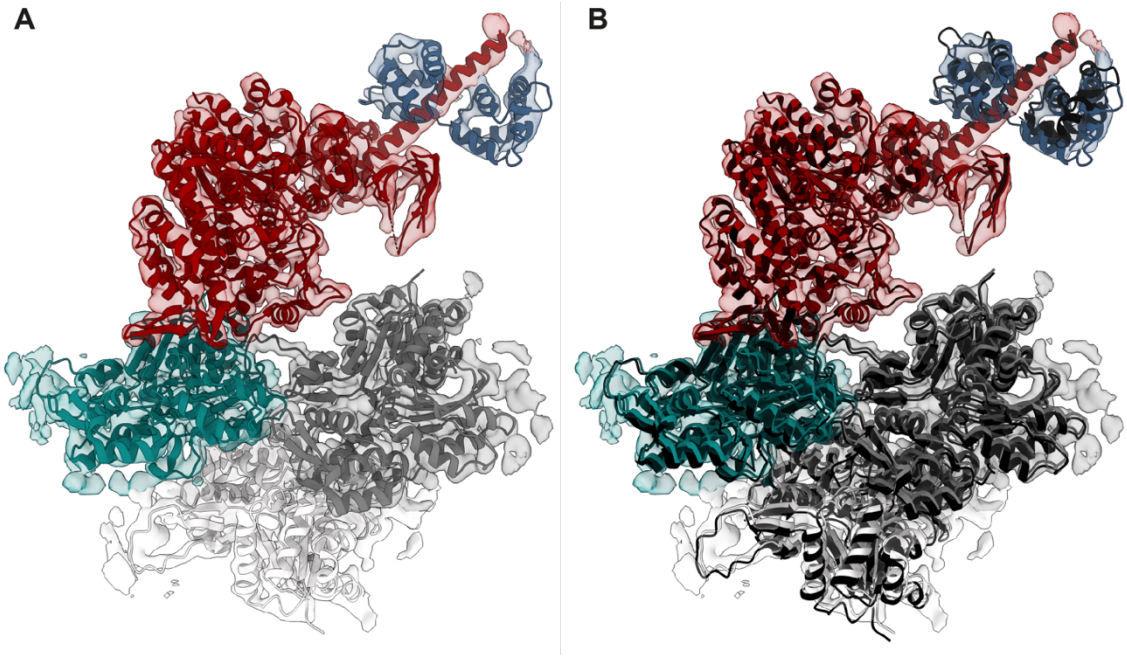

Figure 1 – supplement 3: Fitting of published rigor motor and CaM structure into the cryo-EM motor map obtained in this study

A: *Cryo-EM map of murine Myo5a focusing on the motor + 2IQ and 3 actin subunits, contoured to show 1IQ. Individual chains of the previously solved chicken actomyosin-5a rigor model (PDB: 7PLU, (Pospich et al., 2021)) were rigid fit into this cryo-EM density map. The essential light chain (as in 7PLU) was substituted with the CaM from the CaM-IQ1 crystal structure (PDB: 2IX7, (Houdusse et al., 2006)). Colours as in Figure 1.* ***B:*** *As in* ***A****, but with the previously reported structure (7PLU) overlayed in black. The motor domain of the previously reported structure was rigid fit into the density (displayed in black). All rigid fitting was performed in ChimeraX* (Pettersen et al., 2021).

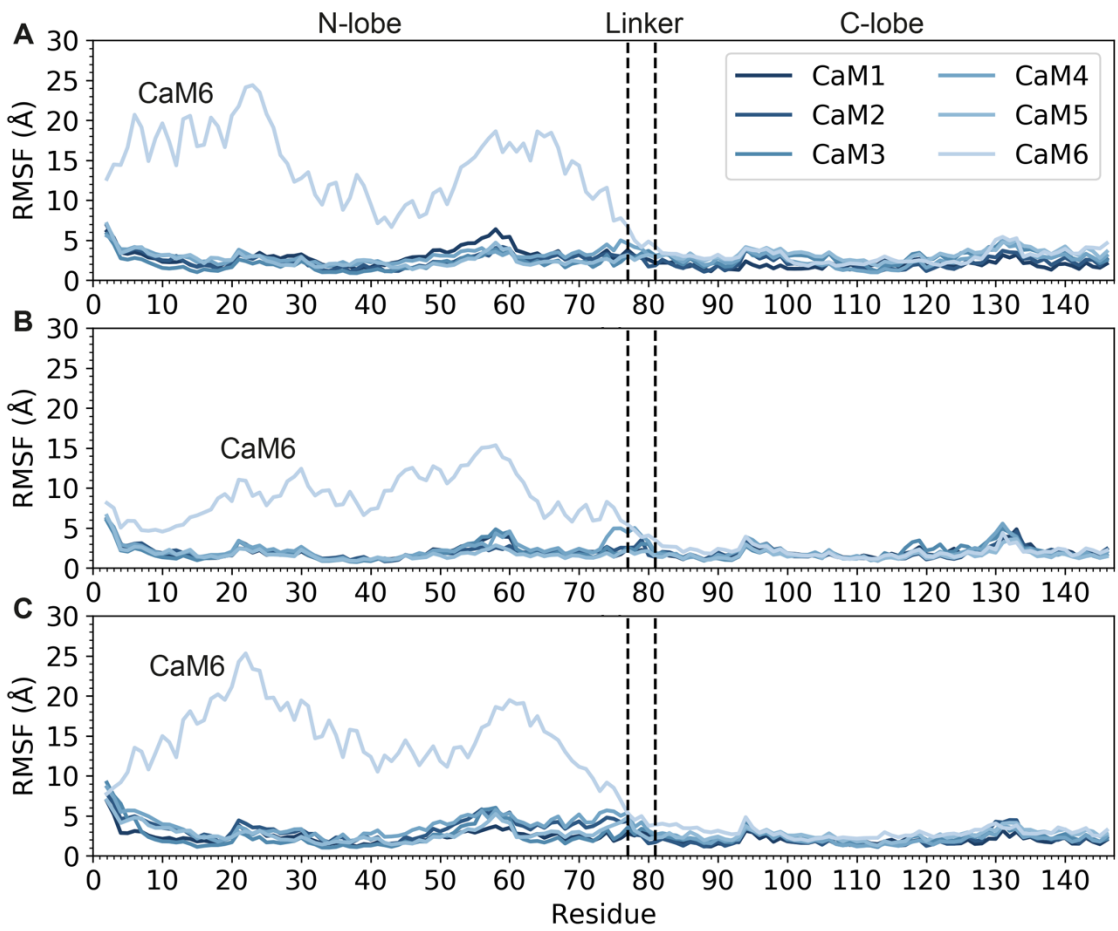

Figure 2: Per residue Root Mean Square Fluctuation plots for CaM1-6

A-C: *Plots of per residue RMSF (Root Mean Square Fluctuation) of CaMs in pseudoatomic model simulations in which the heavy chain is restrained and CaMs are unrestrained. The locations of the N-lobe, linker and C-lobe are indicated. Subfigures are individual repeats. RMSF was calculated in CPPTRAJ (C++ Process Trajectory)* (Roe and Cheatham, 2013).

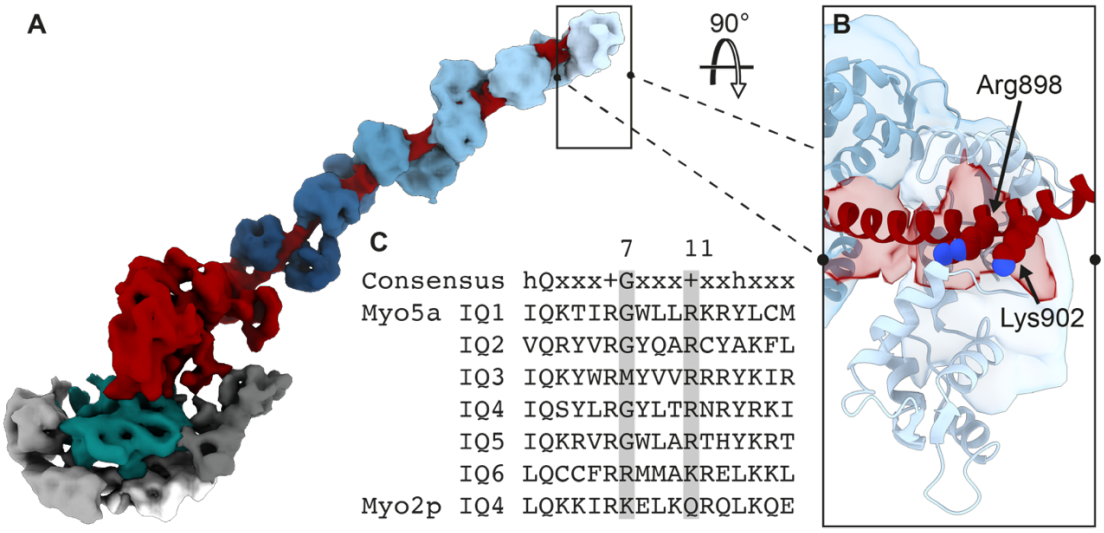

Figure 3: CaM6 N-lobe forms fewer interactions with IQ6 in the heavy chain

A: *cryo-EM map of Myo5a-S1-6IQ, CaM bound to IQ6 (CaM6) boxed.* ***B:*** *90° rotation of boxed region in* ***A,*** *with a pseudo-atomic model fitted to the cryo-EM density. Residues at positions 7 and 11 of IQ6 are displayed as spheres and labelled (Arg898 and Lys902 respectively).* ***C:*** *Sequence alignment of all 6 IQ motifs of murine Myo5a together with IQ4 of Myo2p (PDB:1M46* (Terrak et al., 2003)*). Positions 7 and 11 of each IQ motif are highlighted.*

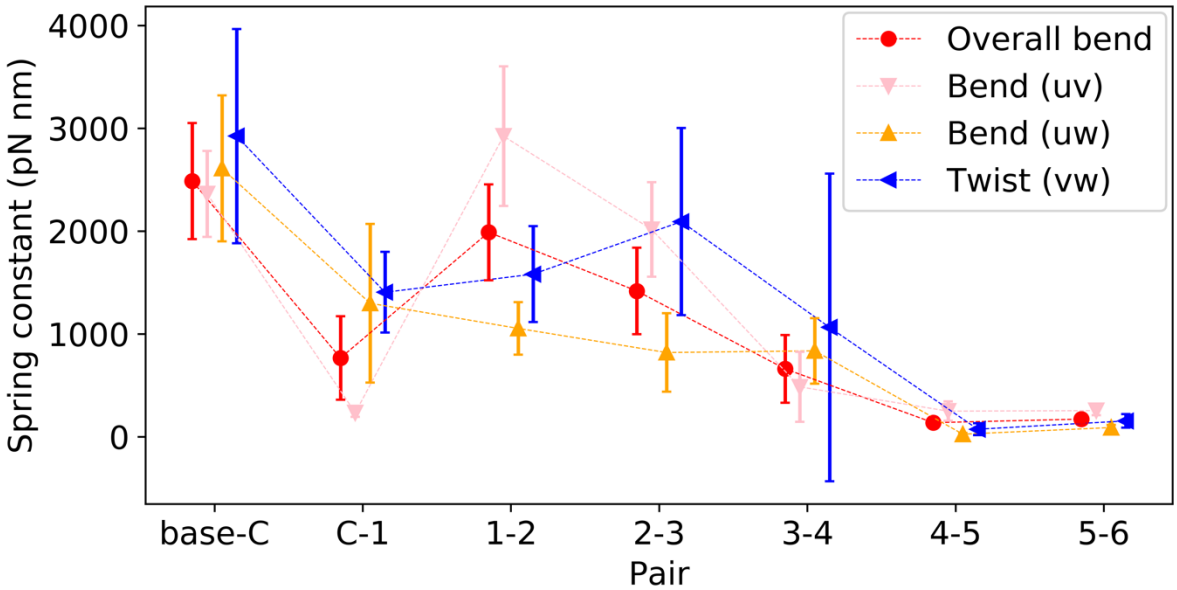

Figure 4: Spring constants for stiffness at hinge points within the lever

Spring constants for hinge points between subdomain pairs (Figure 4 Supplement 1). Overall bend is the average bend constant in the uv and uw planes. Twist is the spring constant in the vw plane. Base = actin binding interface, C = converter, 1 = CaM1, 2 = CaM2, 3 = CaM4, 5 = CaM5, 6 = CaM6 (Figure 4 Supplement 1). Error bars show SD of random error (see Materials and Methods for details).

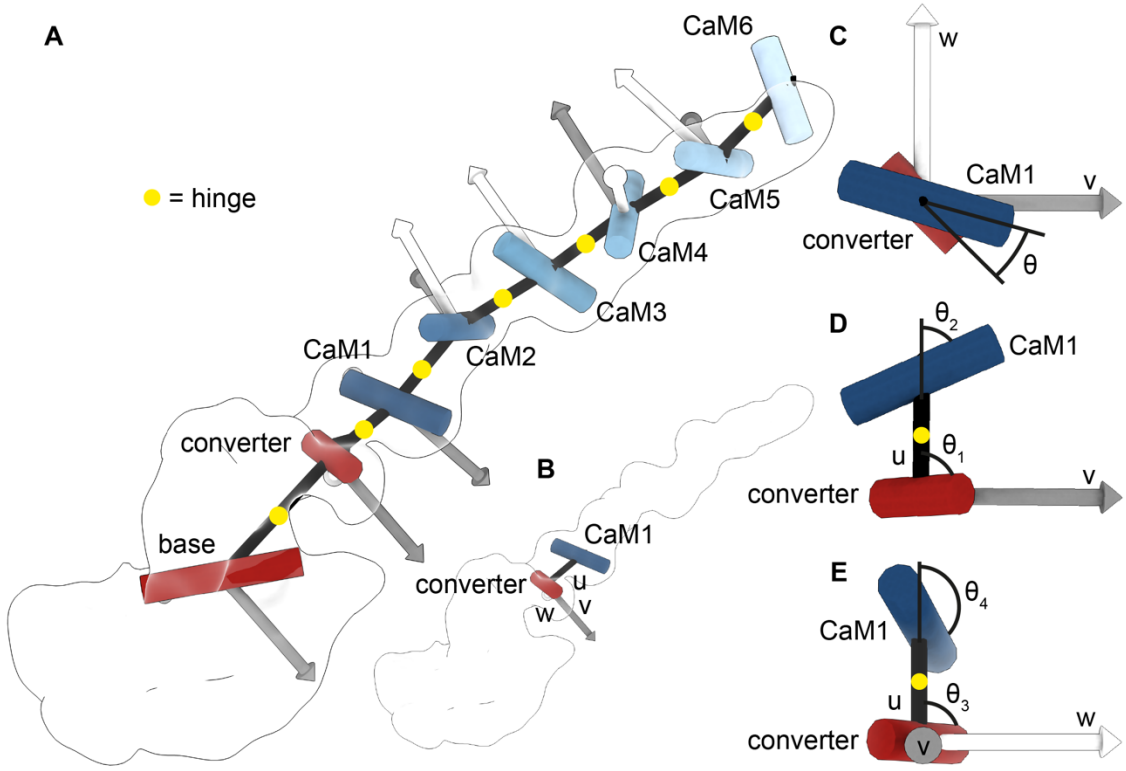

Figure 4 – supplement 1: Coordinates systems for calculating angles between lever subdomain pairs

A: *An example using class D to show the division of subdomains. Vectors representing the subdomains are visualised as cylinders, coloured as in Figure 1A, and displayed within the gaussian filtered cryo-EM map for class D (contour level: 0.25). Local subdomain pair material axes (uvw) are displayed as 3D arrows. u is black, v is grey and w is white. Schematics of hinge points are shown as yellow circles.* ***B:*** *As in* ***A*** *but focusing on the subdomain pair comprising the converter and CaM1, with the local material axes labelled (uvw).* ***C:*** *An example of calculating the angle between a subdomain pair in the vw plane, using the vector representing the converter and the vector representing CaM1.* $\theta_{vw} = \theta$. ***C:*** *An example of calculating the angle between a subdomain pair in the uv plane, using the vector representing the converter and the vector representing CaM1.* $\theta_{uv} = \theta_1 - \theta_2$. ***D:*** *An example of calculating the angle between a subdomain pair in the uw plane, using the vector representing the converter and the vector representing CaM1.* $\theta_{uw} = \theta_3 - \theta_4$.

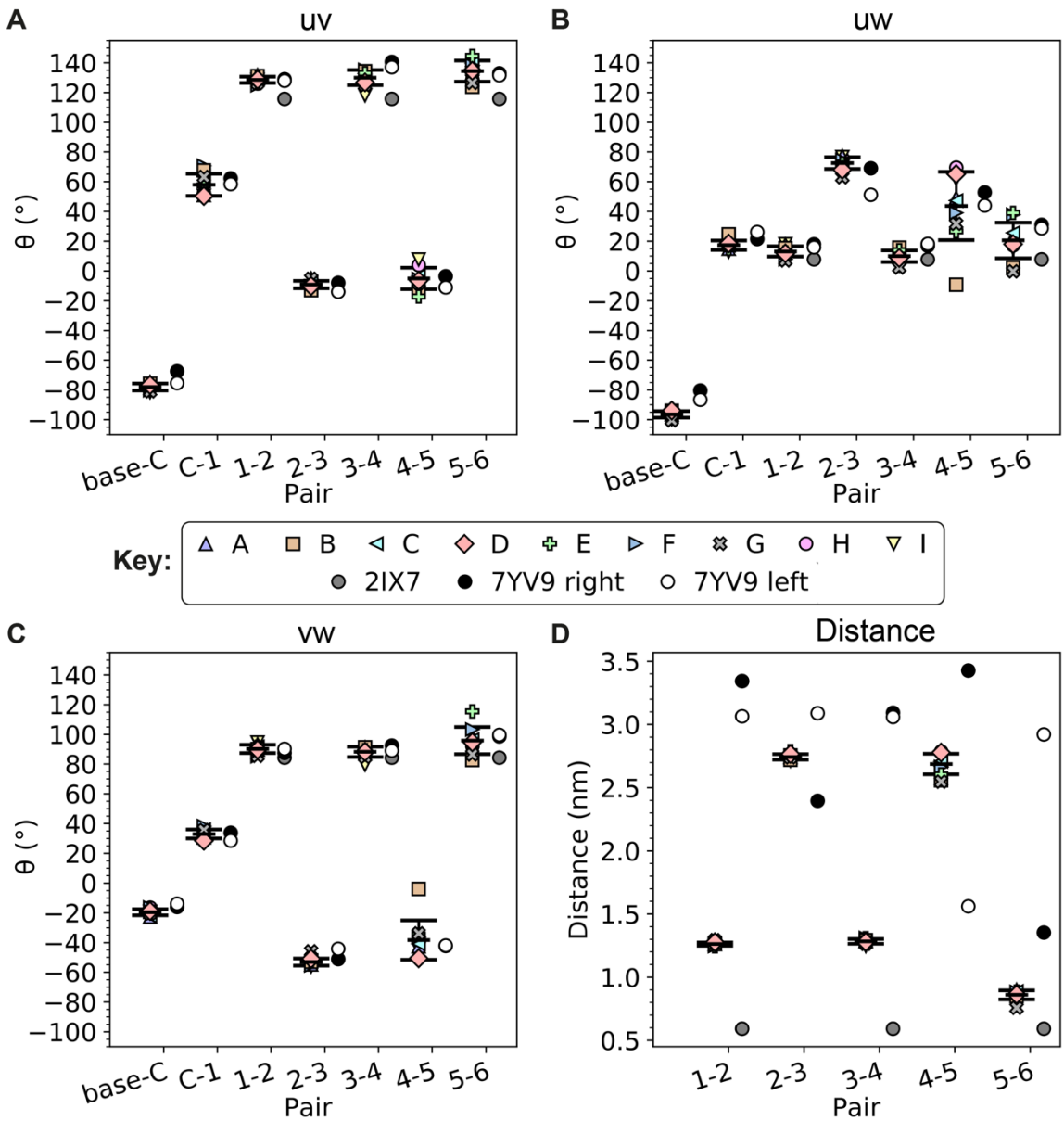

Figure 4 – supplement 2: Angles and distances between lever subdomain pairs

Classes A-H are named and coloured as in Figure 1 Supplement 2. Error bars show the mean and standard deviation of the classes. Conformations of known structures (PDB: 2IX7 and 7YV9 (Houdusse et al., 2006; Niu et al., 2022)) are displayed to the right of our data. Grey circles indicate values for the CaM pair bound to IQ1-2 crystal structure (PDB: 2IX7, (Houdusse et al., 2006)). Black circles indicate conformations of subdomain pairs in the structure of the shutdown state in the head furthest from the C-terminal region of the coiled-coil (right) (PDB: 7YV9 (Niu et al., 2022)*). White circles indicate conformations of subdomain pairs in the structure of the shutdown state in the head closest to the C-terminal region of the coiled-coil (left) (PDB: 7YV9* (Niu et al., 2022)*).* ***A:*** *Angle between lever subdomain pairs in their local uv plane (Figure 4 Supplement 1D).* ***B:*** *Angle between lever subdomain pairs in their local uw plane (Figure 4 Supplement 1E).* ***C:*** *Angle between lever subdomain pairs in their local vw plane (Figure 4 Supplement 1C).* ***D:*** *Distance known interacting residues in the N- and C-lobes of consecutive CaM pairs (measured between the Cα of Ser17 and Asn111, respectively). Base = actin binding interface, C = converter, 1 = CaM1, 2 = CaM2, 3 = CaM4, 5 = CaM5, 6 = CaM6 (Figure 4 Supplement 1).*

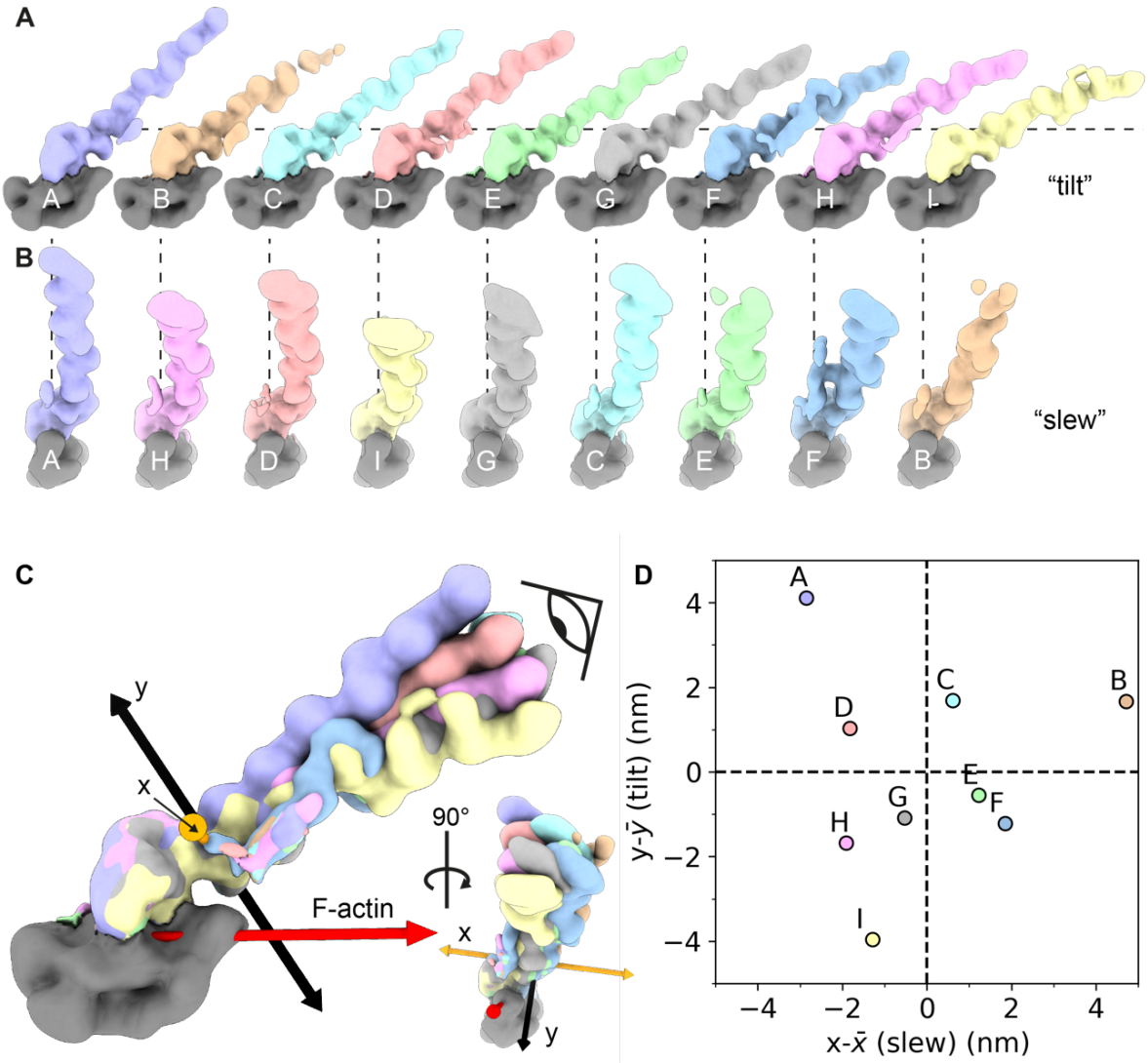

Figure 5: Lever flexibility is directionally isotropic in 3D classes

A: *Post-processed maps of 3D classes in order of lever bend along the F-actin longitudinal axis (tilt).* ***B:*** *post-processed maps of 3D classes in order of lever bend along the F-actin short axis (slew). Maps are Gaussian smoothed (SD 5 Å) (contour level: 0.15).* ***C:*** *Post-processed maps of 3D classes (gaussian filtered SD 5 Å, contour level: 0.15). The coordinate system the stiffness measurements were taken from are displayed as 3D arrows (see Materials and Methods). x-axis = orange arrows, y-axis = black arrows, z = axis mean lever vector (see Materials and Methods). Eye shows viewpoint of* ***D****.* ***D:*** *Plot of the displacement of the end lever in each class from the mean (z) (see Materials and Methods). Changes in x represent motion across the F-actin short axis (slew), changes in y represent motion along the F-actin longitudinal axis (tilt).*

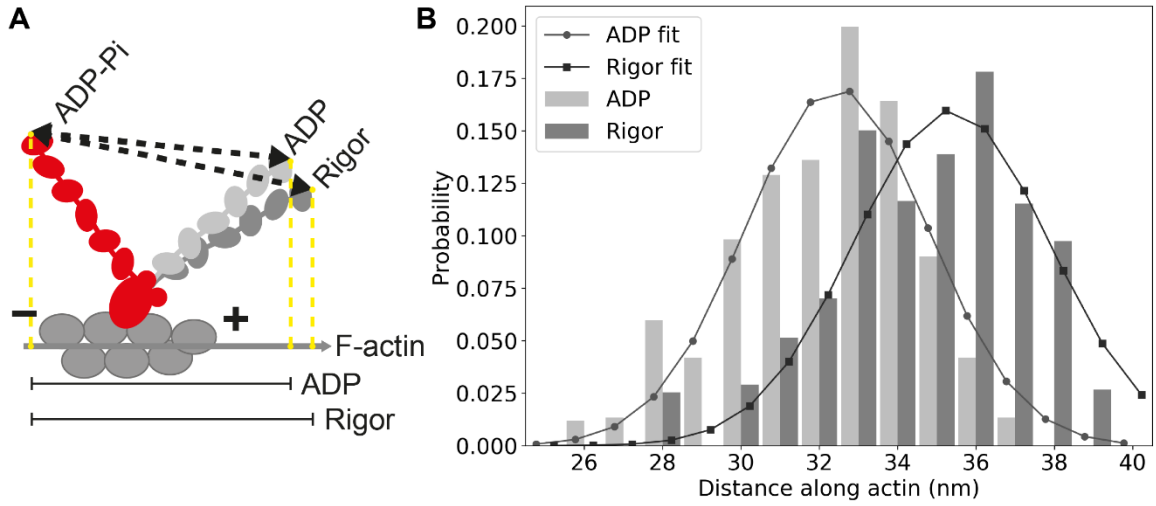

Figure 6: Predicting the working stroke

A: *schematic demonstrating how distances for* ***B*** *were calculated. Distances between lever ends in the modelled ADP-Pi, ADP and rigor conformations are shown as black dashed arrows. Yellow dashed lines show these distances as a translation along the F-actin vector (1st to 13th subunit, grey arrow, see Materials and Methods for details). + indicates the plus end of F-actin, - indicates the minus end of F-actin.* ***B:*** *Histogram of the translation of Myo5a lever ends along F-actin vector from the ADP-P_i conformation to ADP and to rigor (see Materials and Methods for details), and the fitted Gaussian distributions. The probability was calculated using the proportion of particles in each of the cryo-EM 3D classes paired.*

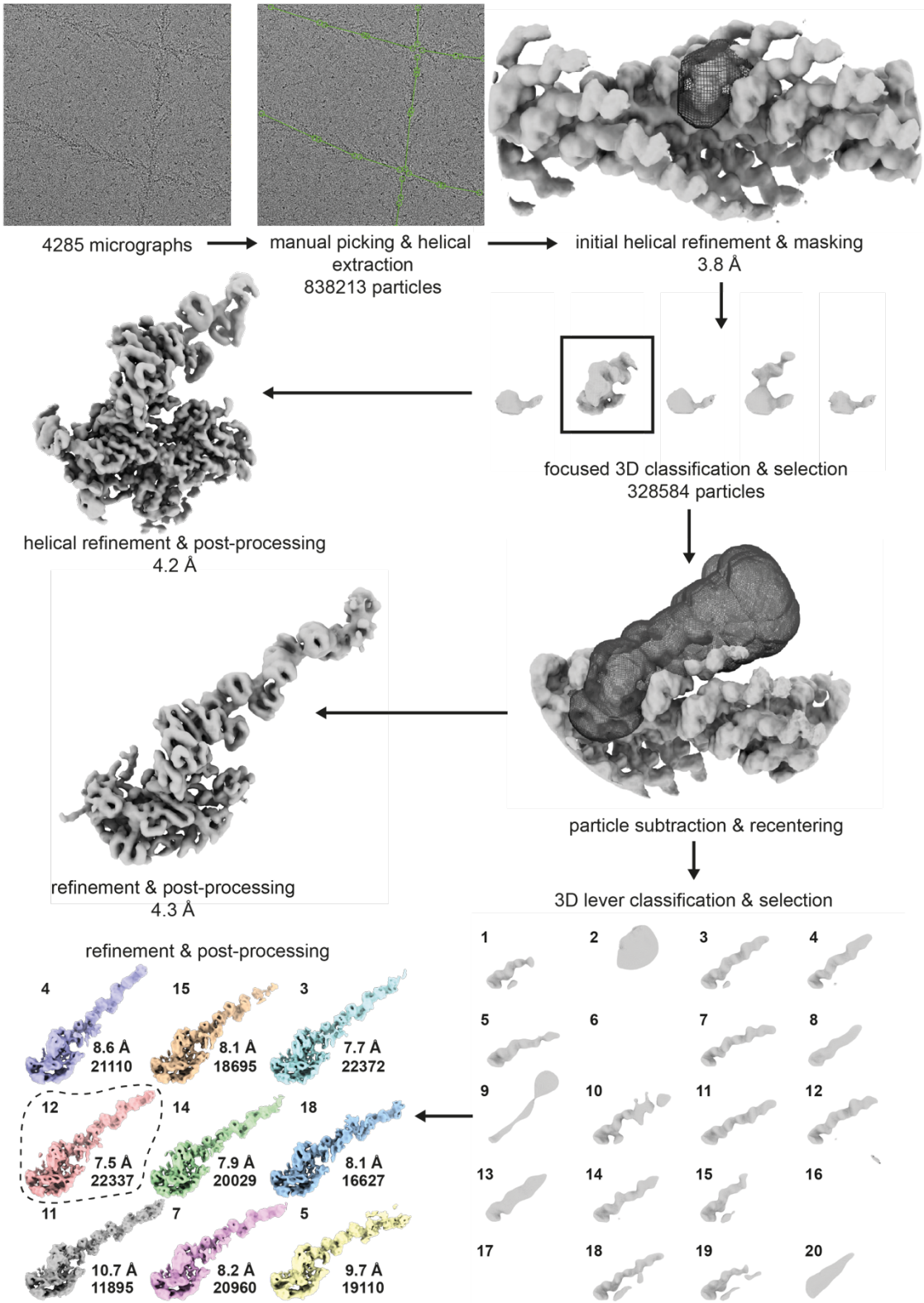

Figure 7: **Processing workflow**

cryo-EM data processing pipeline for Myo5a-S1-6IQ. Showing the number of micrographs used, the particle numbers, corresponding density maps, and masks for particle subtraction. All resolutions quoted are based on global resolution at 0.143 FSC (Fourier Shell Correlation). All resultant density maps displayed were post-processed in DeepEMhancer (Sanchez-Garcia et al., 2021).

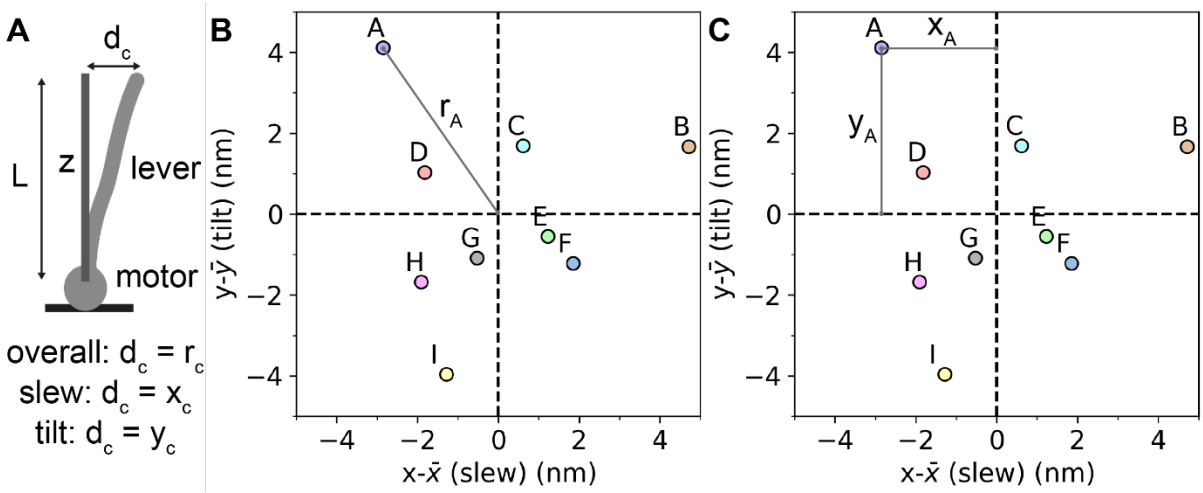

Figure 8: Calculating lever displacement for cantilever bending stiffness
A: *schematic of cantilever-type bending of the lever of Myo5a. d_c is the displacement of the lever from the mean position (z) for each class (c). For the overall bending stiffness the displacement (d_c) was calculated using r_c (**B**). To calculate the bending stiffness in each direction, tilt and slew, the displacement (d_c) was calculated using x_c and y_c, respectively (**C**). L is the mean length of the lever. z is the mean vector of the class lever vectors (converter to CaM6) used as the z axis in **B** and **C**. **B:** demonstration of how r_c were calculated for each cryo-EM class using class A (r_A) and the distribution of end points from Figure 5D. **C:** demonstration of how x_c and y_c were calculated for each cryo-EM class using class A (x_A and y_A, respectively) and the distribution of end points from Figure 5D.*

Table 1: Spring constants for stiffness at hinge points within the lever (2.s.f), ± SD of random error (see Methods for details).

Hinge	Combined spring constant bend (pN nm)	uv spring constant bend (pN nm)	uw spring constant bend (pN nm)	vw spring constant twist (pN nm)
Base-converter	2500 ± 560	2400 ± 420	2600 ± 710	2900 ± 1000
converter-CaM1	770 ± 410	230 ± 39	1300 ± 770	1400 ± 390
CaM1-2	2000 ± 470	2900 ± 680	1100 ± 260	1600 ± 470
CaM2-3	1400 ± 420	2000 ± 460	820 ± 380	2100 ± 910
CaM3-4	660 ± 330	480 ± 340	840 ± 320	1100 ± 1500
CaM4-5	140 ± 54	250 ± 94	24 ± 13	73 ± 57
CaM5-6	170 ± 36	250 ± 45	89 ± 27	150 ± 66

Table 2 - Microscope parameters

Microscope	Titan Krios I
Magnification	75000
Voltage (kV)	300
Electron dose per image ($e^-/Å^2$)	62.66
Exposure time (s)	1.5
Number of fractions	59
Defocus range (μm)	-1.8 to -3.6 (0.3 steps)
Pixel size (Å)	1.065

Table 3: ***MolProbity statistics for the pseudoatomic model of rigor Myo5a-S1-6IQ bound to F-actin***

Atomic model statistics	
MolProbity score	0.73
Clashscore	0.08
Bad bonds (%)	0.04
Bad angles (%)	0.55
Poor rotamers (%)	1.83
Ramachandran favoured (%)	92.37
Ramachandran outliers (%)	0.11
CaBLAM outliers (%)	1.0